ACSNANO

www.acsnano.org

Role of Two-Dimensional Ising Superconductivity in the Nonequilibrium Quasiparticle Spin-to-Charge Conversion Efficiency

Kun-Rok Jeon,*,† Kyungjune Cho,† Anirban Chakraborty, Jae-Chun Jeon, Jiho Yoon, Hyeon Han, Jae-Keun Kim, and Stuart S. P. Parkin*

Cite This: *ACS Nano* 2021, 15, 16819–16827

Read Online

ACCESS | Metrics & More | Article Recommendations | Supporting Information

ABSTRACT: **Nonequilibrium studies of two-dimensional (2D) superconductors (SCs) with Ising spin−orbit coupling are prerequisite for their successful application to equilibrium spin-triplet Cooper pairs and, potentially, Majorana Fermions. By taking advantage of the recent discoveries of 2D SCs and their compatibility with any other materials, we fabricate here nonlocal magnon devices to examine how such 2D Ising superconductivity affects the conversion efficiency of magnon spin to quasiparticle charge in superconducting flakes of 2H-$NbSe_2$ transferred onto ferrimagnetic insulating $Y_3Fe_5O_{12}$. Comparison with a reference device based on a conventionally paired superconductor shows that the $Y_3Fe_5O_{12}$-induced in-plane (IP) exchange spin-splitting in the $NbSe_2$ flake is hindered by its inherent out-of-plane (OOP) spin−orbit field, which, in turn, limits the transition-state enhancement of the spin-to-charge conversion efficiency. Our out-of-equilibrium study highlights the significance of symmetry matching between underlying Cooper pairs and exchange-induced spin-splitting for the giant transition-state spin-to-charge conversion and may have implications toward proximity-engineered spin-polarized triplet pairing via tuning the relative strength of IP exchange and OOP spin−orbit fields in ferromagnetic insulator/2D Ising SC bilayers.**

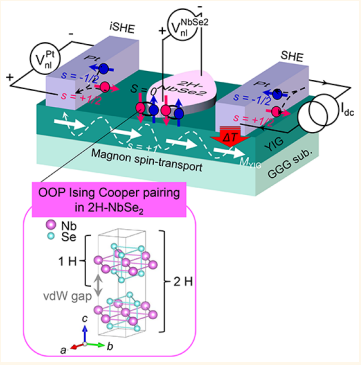

KEYWORDS: *2D superconductor, Ising Cooper pairing, nonequilibrium quasiparticle spin-to-charge conversion, magnon spin transport, IP exchange spin-splitting versus OOP spin−orbit fields*

Injection and excitation of electrons, typically called Bogoliubov quasiparticles (QPs), in a superconductor (SC) with either an external (Zeeman) or internal (exchange) spin-splitting field[1−3] under *nonequilibrium* conditions (*i.e.*, voltage bias or temperature gradient) have been one of the central research topics in superconducting spintronics.[1−7] This is because their exotic transport properties, derived from the superconductivity-facilitated coupling between different nonequilibrium imbalances (*e.g.*, spin, charge, heat, and spin-heat), can considerably improve the functionality and performance of spintronic devices. Various nonequilibrium phenomena mediated by QPs have been observed in SC-based devices with either Zeeman or exchange spin-splitting: long-range spin signals,[8−10] pure thermal spin currents,[11] large (spin-dependent) thermoelectric currents,[12] and spectroscopic evidence of spin-heat transport.[13]

Recently, a magnon spin-transport experiment[14] has reported that the conversion efficiency of thermal-magnon spin to QP charge via an inverse spin-Hall effect (iSHE)[15] in an exchange-spin-split Nb layer can be significantly enhanced by up to 3 orders of magnitude in the normal-to-superconducting transition regime. This giant transition-state QP iSHE has been semi-quantitatively explained in terms of two competing mechanisms of the superconducting coherence versus the exchange-field-frozen QP relaxation. A very recent theory[16] has pointed out that the electron−hole symmetry breaking present in SC/FMI (FMI = ferromagnetic insulator) bilayers mixes the spin and heat imbalances and can cause the enhancement of QP spin accumulation by several orders of

Received: August 19, 2021
Accepted: September 29, 2021
Published: October 1, 2021

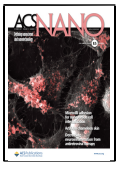

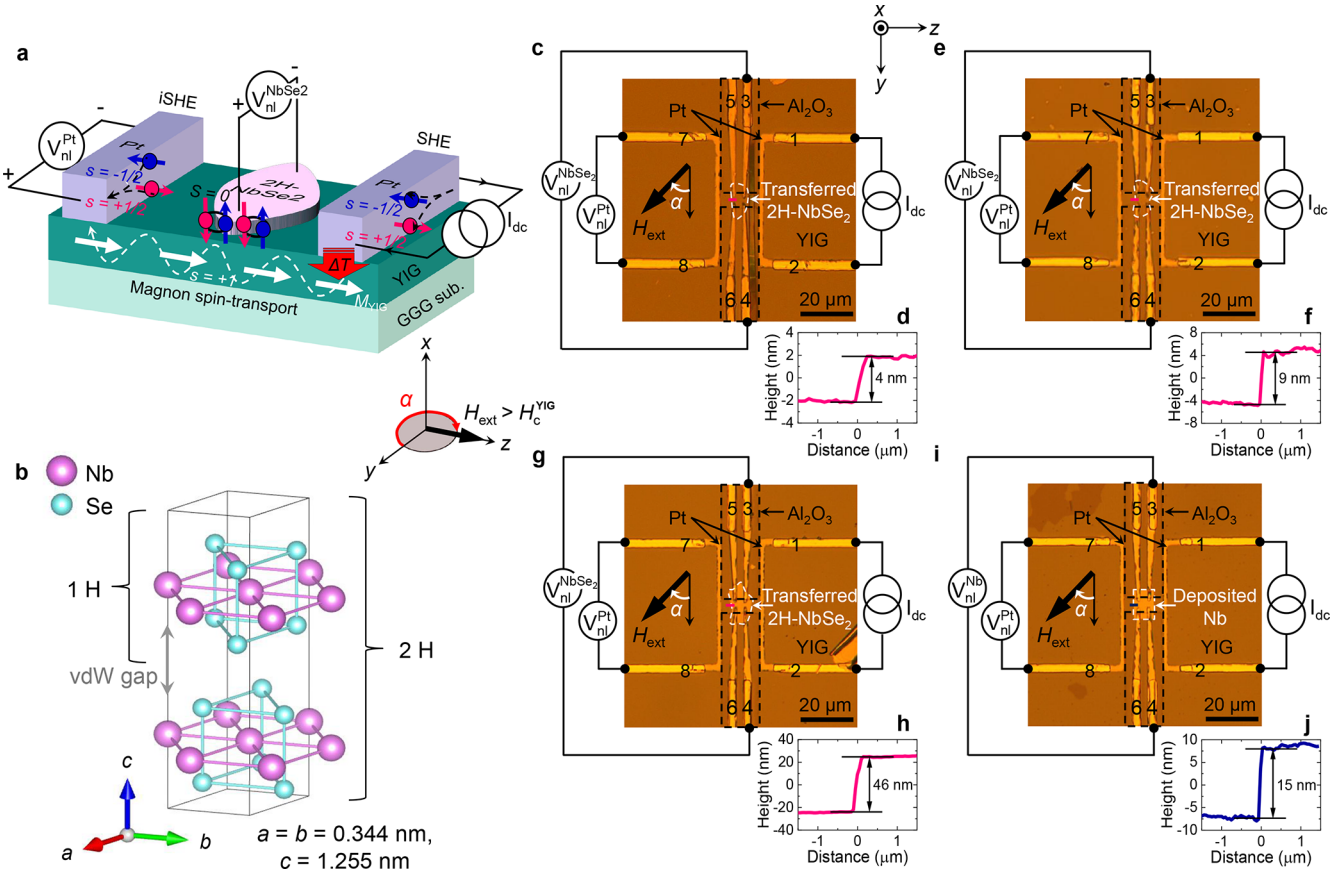

Figure 1. Nonlocal magnon spin-transport device with Ising superconductor. (a) Device layout and measurement scheme. When a dc charge current I_{dc} is applied to the right Pt injector, either electrically or thermally driven magnons accumulate in the ferrimagnetic insulator $Y_3Fe_5O_{12}$ (YIG) underneath and diffuse toward the left Pt detector. These magnon (s = +1) currents are then absorbed by the left Pt detector, resulting in the electron spin accumulation that is, in turn, converted to a nonlocal charge voltage V_{nl}^{Pt} via the inverse spin-Hall effect (iSHE). Such a conversion process also occurs for the central 2H-$NbSe_2$ flake and thereby $V_{nl}^{NbSe_2}$. Note that, unlike spin-singlet (S = 0) Cooper pairs in a coherent ground state, the excited quasiparticles (QPs) can carry spin angular momentum in the superconducting state. How out-of-plane (OOP) Cooper pairing of the 2H-$NbSe_2$ affects the transition-state enhancement of QP iSHE will be discussed in this study. (b) Crystal structure of the 2H-$NbSe_2$, where in-plane inversion symmetry breaking by Se plus spin−orbit coupling of Nb lead to OOP spin-singlet (S = 0) Cooper pairs, constituting Ising superconductivity. (c,e,g,i) Optical micrographs of the fabricated devices. Atomic force microscopy (AFM) scans of the transferred 2H-$NbSe_2$ flakes (d,f,h) and the deposited Nb thin film (j).

magnitude relative to the normal state. Both these studies[14,15] emphasize the crucial role of the spin-splitting of QP density-of-states (DOS) and the resulting electron−hole asymmetry in enhancing the spin sensitivity of the SC detector.[5,15]

The advent of two-dimensional (2D) SCs[17−21] and their compatibility with any other materials via circumventing the need for lattice matching between adjacent material systems provide platforms to explore intriguing physical phenomena in various geometries,[22] including van der Waals (vdW) heterostructures with a twist, and in proximity combination with magnetic vdW flakes and/or thin films.[23,24] Because excited QPs and Cooper pairs in the superconducting condensate state are intimately correlated,[1−6] studies of nonequilibrium QP spin properties in such 2D SCs are of fundamental importance for understanding *equilibrium* spin-polarized triplet Cooper pairing[1−6] and the possible stabilization of Majorana Fermions.[25−27]

2D superconductivity has been recently discovered in monolayer transition metal dicalcogenides (TMDs)[17] such as gated 2H-MoS_2[18,19] and 2H-$NbSe_2$.[20] Interestingly, the in-plane (IP) upper critical field $\mu_0 H_{c2}^{\parallel}$ is found to far exceed the Pauli paramagnetic limit of isotropic Bardeen−Cooper−Schrieffer (BCS) SCs $\mu_0 H_P^{BCS} \approx 1.84 T_c$,[28] where Zeeman spin-splitting fields are the predominant mechanism for Cooper pair breaking in the 2D limit and T_c is the superconducting transition temperature. Such an enhancement of $\mu_0 H_{c2}^{\parallel}$ is explained by Ising spin−orbit coupling (SOC),[17−21] rooted in the broken IP crystal inversion symmetry plus the large SOC due to heavy transition metal atoms in TMDs. The Ising SO field $\mu_0 H_{SO}$ (as large as several hundred Tesla in the monolayer limit)[17−21] strongly pins Cooper pair spins at K and K' points of the hexagonal Brillouin zone to opposite out-of-plane (OOP) directions over IP applied magnetic fields. This stabilizes OOP Cooper pairing and forms so-called Ising superconductivity.[17−21]

We here investigate how the 2D Ising superconductivity influences the transition-state enhancement of magnon spin to QP charge conversion in a superconducting flake of 2H-$NbSe_2$[20,29−31] (Figure 1a) and compare its efficiency with a conventional superconducting thin film of Nb[14] (BCS SC). We first demonstrate that the normal-state spin-to-charge conversion functionality of the 2H-$NbSe_2$ flake can be *4 times more*

https://doi.org/10.1021/acsnano.1c07192
ACS Nano 2021, 15, 16819−16827

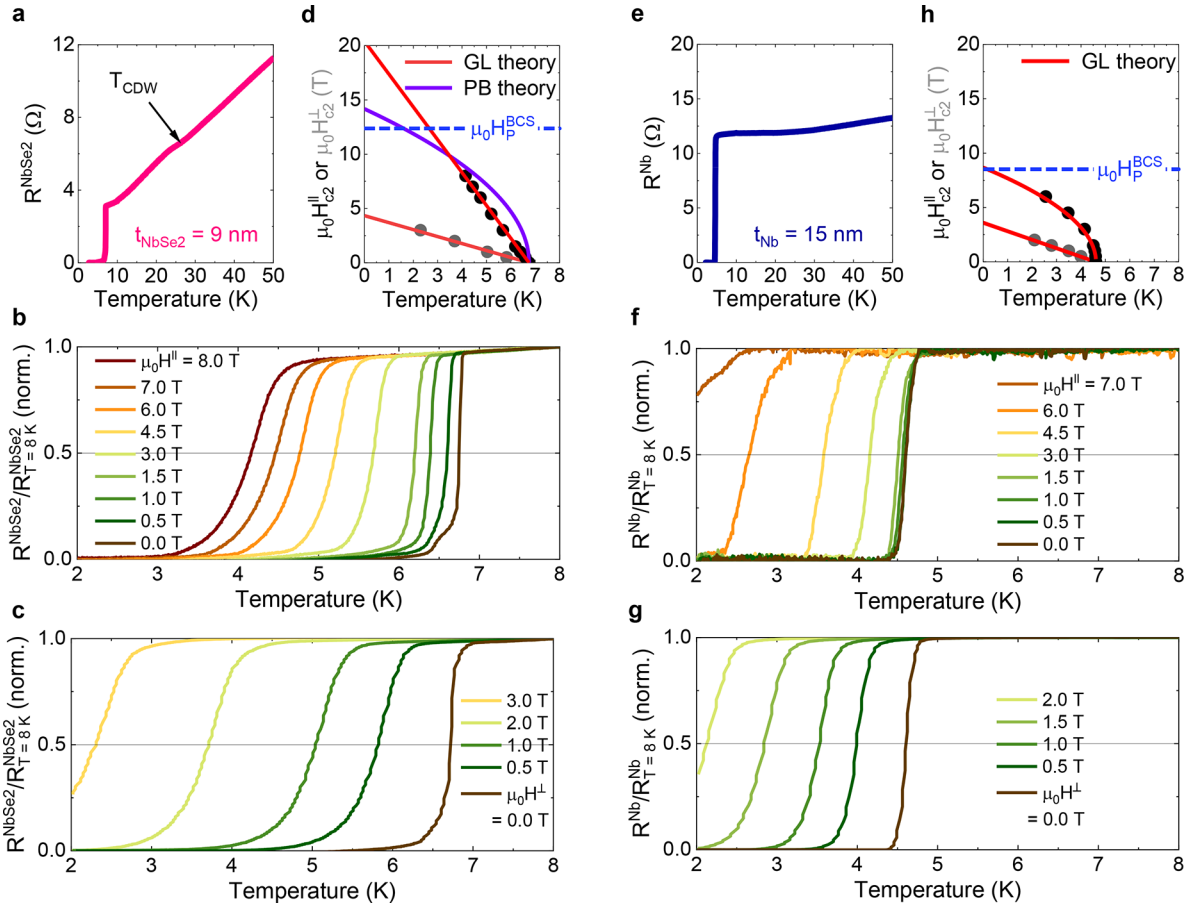

Figure 2. Electrical characterization of the transferred 2H-$NbSe_2$ flake. (a) 2H-$NbSe_2$ resistance R^{NbSe_2} as a function of temperature, T, for the transferred 2H-$NbSe_2$ flake (t_{NbSe_2}= 9 nm) measured using a 4-terminal current−voltage method (using leads 3−6 in Figure 1e). Typical R^{NbSe_2}−T curves measured by applying an external magnetic field either parallel $\mu_0 H^{\parallel}$ (b) or perpendicular $\mu_0 H^{\perp}$ (c) to the interface plane. The T-dependent IP (OOP) upper critical field $\mu_0 H_{c2}^{\parallel}$ ($\mu_0 H_{c2}^{\perp}$) is determined from the point where R = 0.5$R_{T=8K}$. (d) Summary of the $\mu_0 H_{c2}^{\parallel}(T)$ and $\mu_0 H_{c2}^{\perp}(T)$ data. The blue dashed line represents the Pauli paramagnetic limit $\mu_0 H_P^{BCS} \approx 1.84 T_c$.[28] The red and violet solid lines in (b) are theoretical fits using Ginzburg−Landau (GL)[39] and pair breaking (PB)[20] theories, respectively. (e−h) Data equivalent to (a)−(d) but for the t_{Nb} = 15 nm reference device (Figure 1j).

efficient than that of the Nb film. We then find distinctively different transition-state conversion behaviors (*e.g.*, modest transition-state enhancement, rather weak thickness dependence) in the 2H-$NbSe_2$ and attribute these to OOP Cooper pairing that hampers proximity penetration of IP exchange spin-splitting from the adjacent ferrimagnetic insulating $Y_3Fe_5O_{12}$. Notably, the maximum enhancement of spin-to-charge conversion appears at a critical thickness over which the IP crystal symmetry is recovered (equivalently, OOP Ising pairing is no longer protected), allowing the IP exchange field to penetrate. This provides a guideline as to how to tune the relative strength of these two phenomena for a desired proximity effect.[32,33] We believe that, along with recent advances in 2D SCs of various intriguing properties (*e.g.*, type-I/-II Ising, Rashba, topological SCs),[22,34] our approach helps find right material combinations for developing superconducting spintronic devices over conventional BCS SCs.

RESULTS AND DISCUSSION

Our nonlocal magnon spin-transport devices (Figure 1a) are composed of two identical Pt electrodes and a central 2-H $NbSe_2$ flake transferred onto 200 nm thick single-crystalline $Y_3Fe_5O_{12}$ (YIG) films (see Methods and Supplementary section 1 for details), which are grown by liquid phase epitaxy on a (111)-oriented single-crystalline $Gd_3Ga_5O_{12}$, (GGG) wafer. Bulk 2H-$NbSe_2$ is a layered type-II SC, having anisotropy[29] in both the IP (OOP) coherence length $\xi_{SC}^{\parallel}$($\xi_{SC}^{\perp}$) ≈ 10 (3) nm and the IP (OOP) London penetration depth $\lambda_L^{\parallel}$ ($\lambda_L^{\perp}$) ≈ 70 (230) nm at zero temperature T = 0. As shown in Figure 1b, it has a hexagonal crystal structure with lattice constants, $a = b \approx 0.3$ nm and $c \approx 1.3$ nm and each unit cell consists of two AB stacked $NbSe_2$ layers.[30,31] On a single-piece YIG film, we prepared several independent devices with different 2H-$NbSe_2$ flake thicknesses t_{NbSe_2} (Figure 1c−h) as well as reference devices in which Nb thin film is directly deposited[14] (Figure 1i,j). The Nb thickness t_{Nb} is fixed at 15 nm, which is comparable to its dirty-limit coherence length ξ_{Nb}, so that the YIG-induced exchange spin-splitting-field can penetrate the Nb layer while retaining the superconducting coherence, thereby maximizing the transition-state QP iSHE.[14]

In this device structure (Figure 1c,e,g,i), we pass a dc current I_{dc} through one Pt electrode (using leads 1 and 2) while measuring the IP magnetic-field-angle α dependence of the

https://doi.org/10.1021/acsnano.1c07192
ACS Nano 2021, 15, 16819−16827

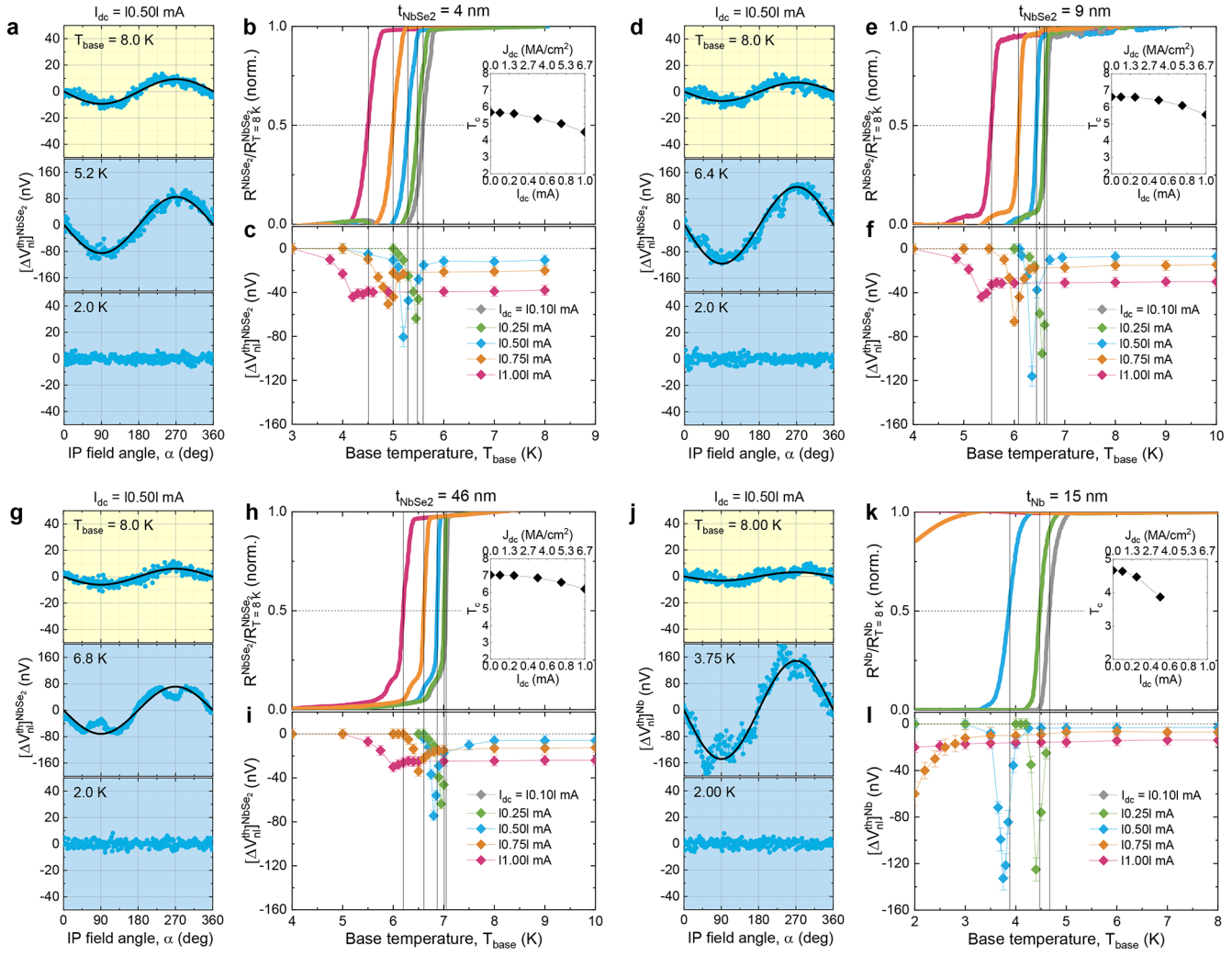

Figure 3. Enhancement of nonlocal signals in the transition state of the 2H-$NbSe_2$ detector. (a,d,g) Thermally driven nonlocal voltages $[\Delta V^{th}_{nl}(\alpha)]^{NbSe_2}$ as a function of IP field angle α for the t_{NbSe_2}= 4, 9, and 46 nm devices, taken at I_{dc} = I0.5I mA around the superconducting transition, T_c, of the 2H-$NbSe_2$. The black solid lines are sin(α) fits. Note that dips in $[\Delta V^{th}_{nl}]^{NbSe_2}$ at $\alpha \approx 90°$ and 270° near T_c which are pronounced for a thicker flake arise from Abrikosov-vortex-flow-driven *spin-independent* Hall effect[14] under a transverse magnetic field that is close to the upper critical field $\mu_0 H_{c2}$ of type-II SC (*i.e.*, vortex melting field). (b,e,h) Normalized 2H-$NbSe_2$ resistance $R^{NbSe_2}/R^{NbSe_2}_{T=8K}$ *versus* T_{base} plots for the t_{NbSe_2}= 4, 9, and 46 nm devices, measured using a four-terminal current−voltage method (using leads 3−6 in Figure 1c,e,g) with varying I_{dc} in the Pt injector. The critical temperature T_c is defined as the point where $R^{NbSe_2} = 0.5R^{NbSe_2}_{T=8K}$. The inset summarizes the measured T_c as a function of I_{dc} (or J_{dc}). (c,f,i) Estimated magnitude of $[\Delta V^{th}_{nl}]^{NbSe_2}$ as a function of T_{base} for the t_{NbSe_2}=4, 9, and 46 nm devices. (j−l) Data equivalent to (a)−(c) but for the t_{Nb} = 15 nm reference device.

nonlocal open-circuit voltages $[V^{Pt}_{nl}(\alpha), V^{NbSe_2(or\,Nb)}_{nl}(\alpha)]$ using the other Pt electrode (leads 7 and 8) and the central $NbSe_2$ (or Nb) (leads 3 and 4). Since we apply an external IP magnetic field $\mu_0 H_{ext}$ = 5 mT that is larger than the coercive field $\mu_0 H^{YIG}_c$ of YIG, α is simply defined as the relative angle of $\mu_0 H_{ext}$ (//M_{YIG}) to the long axis of the two Pt electrodes which are collinear.[14] The total voltage measured across the detector is then given by $V^{tot}_{nl} = \Delta V^{el}_{nl} + \Delta V^{th}_{nl} + V_0$. Here, ΔV^{el}_{nl} and ΔV^{th}_{nl} developed via iSHE (spin-to-charge conversion)[15] in the detector are proportional to the magnon spin current and accumulation created electrically [SHE (charge-to-spin conversion)[15] ∝ I_{dc}] and thermally [spin-Seebeck effect (SSE, heat-to-spin conversion)[35] ∝$(I_{dc})^2$], respectively.[14,35] By inverting the polarity of I_{dc}, one can determine the magnitude of each component based on their characteristic angular dependences:[14,36]

$$\Delta V^{el}_{nl} = \frac{[V^{tot}_{nl}(+I_{dc}) - V^{tot}_{nl}(-I_{dc})]}{2} \propto \sin^2(\alpha)$$

and

$$\Delta V^{th}_{nl} = \frac{[V^{tot}_{nl}(+I_{dc}) + V^{tot}_{nl}(-I_{dc})]}{2} - V_0 \propto \sin(\alpha)$$

where V_0 is a spin-independent offset voltage. Below, our discussion will focus on ΔV^{th}_{nl}, since it remains detectably large at low T for reasonable $|I_{dc}|$ such that Joule heating does not destroy the superconducting phase of the 2H-NbSe flake (or Nb thin film).

https://doi.org/10.1021/acsnano.1c07192
ACS Nano 2021, 15, 16819−16827

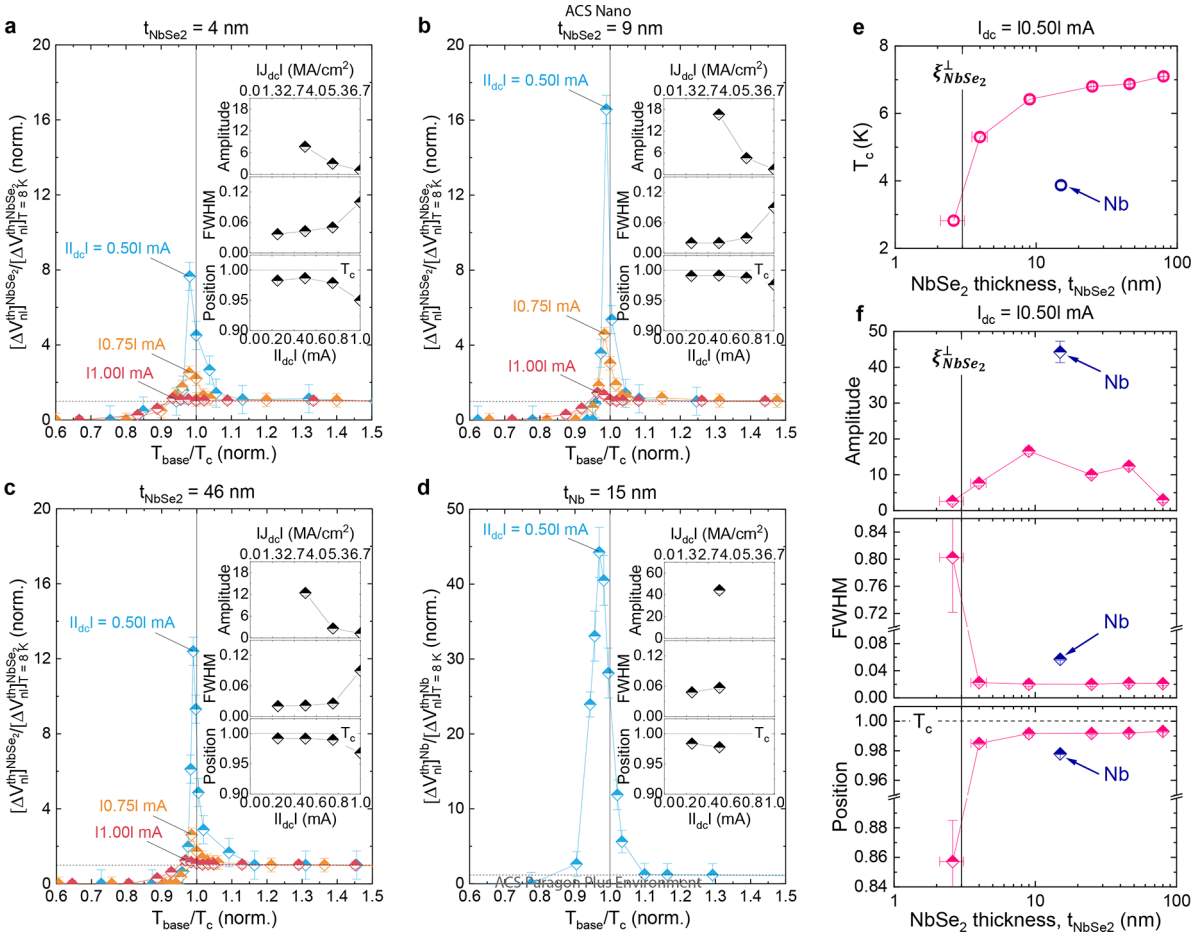

Figure 4. 2H-$NbSe_2$ thickness dependence of the transition-state enhancement and comparison with the Nb detector. (a–c) $\lceil\Delta V_{nl}^{th}\rceil^{NbSe_2}/\Delta\lceil V_{nl}^{th}\rceil^{NbSe_2}_{T=8K}$ *versus* T_{base}/T_c plot for the t_{NbSe_2}=4, 9, and 46 nm devices. Each inset displays the $|I_{dc}|$ (or $|J_{dc}|$) dependence of the peak amplitude, width, and position. (d) Data equivalent to (a) but for the t_{Nb} = 15 nm device. Note that unlike the amplitude, the width and position can be approximately estimated based on data below T_c (Figure 3c,f,i,l) where the transition-state enhancement of QP iSHE provides a detectable amplitude of $\lceil\Delta V_{nl}^{th}\rceil^{NbSe_2}$. (e) t_{NbSe_2}-dependent T_c. (f) t_{NbSe_2}-dependent peak amplitude, width, and position. Abrupt changes of T_c, peak width and position below t_{NbSe_2}= 3 nm, coinciding with the OOP coherence length $\xi^{\perp}_{NbSe_2}$ (black vertical line in e and f), are likely due to thermal-fluctuation-enhanced T_c suppression at the 2D limit.[20,39] Detailed results of the t_{NbSe_2} = 2.5 nm device can be found in Supplementary section 3. In (e) and (f), data from the t_{Nb} = 15 nm reference device are also included for quantitative comparison.

Let us first discuss the electrical transport properties of the transferred 2H-$NbSe_2$ flake. In the plot of its resistance R^{NbSe_2} versus temperature T (Figure 2a) for t_{NbSe_2} = 9 nm, a resistance anomaly appears around 26 K, which is indicative of its phase transition from a normal metal to an incommensurate charge density wave (CDW) phase.[37] Note that the strongly suppressed CDW phase transition temperature, T_{CDW} = 26 K for our t_{NbSe_2} = 9 nm flake, is presumably due to the proximity coupling of the CDW with the magnetic order of YIG. In analogy with the Pauli effect[28] in conventional SCs, the Zeeman (or exchange) energy competes with the CDW condensation energy and hence T_{CDW} is predicted to decrease in the presence of external (and/or internal) spin-splitting fields.[38] As T is reduced further, 2H-$NbSe_2$ becomes superconducting below ~6.75 K. From the T-dependent upper critical field (Figure 2d), that is obtained by applying an external magnetic field either parallel $\mu_0 H^{\parallel}$ (Figure 2b) or perpendicular $\mu_0 H^{\perp}$ (Figure 2c) to the interface plane, we find $\xi^{\parallel}_{NbSe_2} \approx$ 8 nm and $\xi^{\perp}_{NbSe_2} \approx$ 3 nm using Ginzburg–Landau (GL) theory[39] (see Methods for a detailed discussion), so confirming the anisotropic superconducting state of 2H-$NbSe_2$.[29] The extrapolated value of $\mu_0 H^{\parallel}_{c2}$ at lower T goes beyond $\mu_0 H_P^{BCS}$ = 12.4 T. Because the t_{NbSe_2} = 9 nm flake corresponds to 7× the unit cell and is much smaller than $\lambda_L^{\perp} \approx$ 230 nm, neither the IP crystal inversion symmetry nor orbital effect (*i.e.*, interlayer Meissner screening current) is fully recovered.[17] So Ising Cooper pairing[17−21] would account for the increase of $\mu_0 H^{\parallel}_{c2}$ over $\mu_0 H_P^{BCS}$. Note that a rather linear $\mu_0 H^{\parallel}_{c2}(T)$ behavior for the intermediate t_{NbSe_2} = 9 nm suggests that not only Ising SOC[20] but also Abrikosov vortex occupation[39] causes Cooper pair breaking (see Methods for details). These multiple characteristics are a measure of the high quality of our transferred 2H-$NbSe_2$ flake. In contrast, the deposited Nb thin film of t_{Nb} = 15 nm has isotropic coherence lengths $\xi^{\parallel}_{Nb} \approx \xi^{\perp}_{Nb} \approx$ 12–13 nm (Figure 2h) and its low-T $\mu_0 H^{\parallel}_{c2}$ value is below $\mu_0 H_P^{BCS}$= 8.3 T (Figure 2f–h), as would be expected from an isotropic BCS SC.

https://doi.org/10.1021/acsnano.1c07192
ACS Nano 2021, 15, 16819–16827

We now focus on how the conversion efficiency of magnon-carried spin to QP charge varies when the 2H-$NbSe_2$ becomes superconducting. Figure 3a,d,g shows the thermally driven nonlocal signal $\lceil \Delta V_{nl}^{th} \rceil^{NbSe_2}$ for the t_{NbSe_2} = 4, 9, and 46 nm devices at various base temperatures T_{base} around the superconducting transition T_c. In the normal state ($T_{base}/T_c > 1$), a negative $\lceil \Delta V_{nl}^{th} \rceil^{NbSe_2}$ (<0) of a few tens of nanovolts is observed for I_{dc} = |0.5| mA (J_{dc} = |3.0| MA/cm^2). Given $\lceil \Delta V_{nl}^{th} \rceil^{Pt} > 0$ (Supplementary section 2) and $\lceil \Delta V_{nl}^{th} \rceil^{Nb} < 0$ (Figure 3j), this indicates that the 4d heavy element Nb, having a negative spin-Hall angle θ_{SH} (<0), governs spin-to-charge conversion characteristics in the normal-state 2H-$NbSe_2$. Upon entering the superconducting state ($T_{base}/T_c < 1$), a clear enhancement of $\lceil \Delta V_{nl}^{th} \rceil^{NbSe_2}$ up to around 100 nV appears immediately below T_c ($T_{base}/T_c \approx 0.99$) and then it decays toward zero, deep into the superconducting state. It is noteworthy that, for the normal state ($T_{base} > T_c$), $\lceil \Delta V_{nl}^{th} \rceil^{NbSe_2}$ of the transferred 2H-$NbSe_2$ flakes go beyond $\lceil \Delta V_{nl}^{th} \rceil^{Nb}$ of the deposited Nb film, in particular, the t_{NbSe_2} = 2.5 nm device reveals *4 times greater* signals (Supplementary section 3), indicating high spin mixing conductance and spin transparency at the interface between our transferred 2H-$NbSe_2$ flakes and YIG film.

We systematically measure the T_{base} dependence of the normalized $R^{NbSe_2}/R^{NbSe_2}_{T=8K}$ (Figure 3b,e,h) and $\lceil \Delta V_{nl}^{th} \rceil^{NbSe_2}$ (Figure 3c,f,i) with varying I_{dc} in the Pt injector. The results are qualitatively similar to the magnon devices with Nb detectors[14] and also to the t_{Nb} = 15 nm reference device studied here (Figure 3j–l). As I_{dc} increases, T_c of the 2H-$NbSe_2$ detector is progressively reduced (inset of Figure 3c,f,i) and the transition width broadens. As a result of this depressed superconductivity, caused by the combined effect of more populated spin-polarized QPs[5] and increased heat dissipation in the 2H-$NbSe_2$ at a high I_{dc}, a peak of the $\lceil \Delta V_{nl}^{th} \rceil^{NbSe_2}$ enhancement occurring in the vicinity of T_c (Figure 3c,f,i) shifts to a low T_{base} and the enhancement regime widens. These demonstrate that the spin-to-charge conversion efficiency indeed rises when mediated by QPs in the transition state of 2H-$NbSe_2$/YIG bilayer, that is the enhanced spin-detection functionality of a 2D Ising SC in the normal-to-superconducting transition regime.

We next plot the normalized voltages $\lceil \Delta V_{nl}^{th} \rceil^{NbSe_2}/\lceil \Delta V_{nl}^{th} \rceil^{NbSe_2}_{T=8K}$ (Figure 4a–c) and $\lceil \Delta V_{nl}^{th} \rceil^{Nb}/\lceil \Delta V_{nl}^{th} \rceil^{Nb}_{T=8K}$ (Figure 4d) as a function of the normalized temperature T_{base}/T_c for a quantitative analysis. With increasing I_{dc}, the peak amplitude strongly diminishes, the full-width-at-half-maximum (fwhm) broadens, and the peak position is away from T_c (inset of Figure 4a–d). In addition to these generic features, one can find important quantitative differences between the 2H-$NbSe_2$ and Nb detectors[14] from the thickness dependence of the amplitude, fwhm and position (Figure 4f).

First, the enhancement amplitude attained in the 2H-$NbSe_2$ detectors is relatively small ($\lceil \Delta V_{nl}^{th} \rceil^{NbSe_2}/\lceil \Delta V_{nl}^{th} \rceil^{NbSe_2}_{T=8K} \leq 12$) compared with the t_{Nb} = 15 nm reference device with a similar lateral dimension, even though the 2H-$NbSe_2$ flakes (*e.g.*, t_{NbSe_2} = 4, 9 nm) possess a higher T_c in thinner layers (Figure 4e). Second, the peak width and position abruptly change across 3 nm, coinciding with $\xi^{\perp}_{NbSe_2}$ (black vertical line in Figure 4e,f) below which thermal-fluctuation-enhanced T_c suppression at the 2D limit is expected,[20,39] and they become almost t_{NbSe_2}-independent for thicker flakes. Note that the Nb dectectors[14] reveal a monotonic narrowing of fwhm and a peak shift closer to T_c with increasing t_{Nb}. Third, unlike the Nb detectors,[14] the maximum enhancement in the spin-to-charge conversion does not appear at $t_{NbSe_2} \approx \xi^{\perp}_{NbSe_2}$ and the t_{NbSe_2}-dependent enhancement is rather weak.

To account for these distinctively different conversion phenomena, we consider the layer thickness-dependent Ising superconductivity.[20,40] For a few monolayer 2H-$NbSe_2$, the IP crystal inversion symmetry is strongly broken by Se atoms (Figure 1b) and thus OOP Cooper pairing is protected and stabilized by the resulting Ising SO-field (76 meV in the monolayer limit).[20,41] In this regime, the YIG-induced IP exchange field (<1 meV)[14,41] hardly spin-splits the QP DOS of the 2H-$NbSe_2$ and the transition-state enhancement of QP iSHE thus relies mostly on the superconducting-coherence-relevant resonant absorption,[14,16,42] leading to a modest enhancement. As the flake becomes thicker, the IP bulk crystal inversion symmetry is restored, which weakens the OOP Ising pairing and, in turn, enables the YIG-induced IP exchange field to propagate through. This explains why we obtain the maximum enhancement of the transition-state QP iSHE at t_{NbSe_2} = 9 nm ($>\xi^{\perp}_{NbSe_2}$). Note that, as a critical thickness value that is necessary to fully restore the IP bulk inversion symmetry (equivalently, to diminish Ising pairing) is larger than the coherence length, beyond this critical value, proximity extension of the YIG-induced IP exchange spin-splitting over the entire 2H-$NbSe_2$ layers is not very effective, limiting the enhancement amplitude. Furthermore, a Γ-centered Se-electron Fermi pocket, constituting a second band with a smaller superconducting gap, emerges in the 2H-$NbSe_2$ thicker than a few monolayers.[43] This second band whose gap energy seems weakly dependent on t_{NbSe_2}[43] can provide another path for spin-polarized QPs to enter the 2H-NbSe detector, effectively weakening the t_{NbSe_2}-dependent transition-state enhancement.

Our out-of-equilibrium study highlights the importance of symmetry matching between underlying Cooper pairs and exchange-induced spin-splitting for the giant transition-state enhancement of QP iSHE.[14,16] Based on this, we would predict a greater transition-state QP iSHE, for instance, in $MnPS_3$/$NbSe_2$ bilayers, where exchange spin-splitting[44] and SO fields are both OOP and thus match in the symmetry each other. Similarly, Rashba SC/YIG bilayers, where the Rashba SC has IP SO-fields,[34] would be another symmetry-matching combination. Our results may also provide a guideline for the proximity engineering of hybrid quantum materials that allow for exotic quantum phases (*e.g.*, topological superconductivity with spin-polarized triplet pairs and/or Majorana zero modes)[25−27] at zero field in equilibrium.

CONCLUSIONS

Our magnon spin-transport experiments with 2H-$NbSe_2$ detectors have shown that OOP Cooper pairing of Ising SC, derived by IP inversion symmetry breaking and strong SOC, hinders the proximity propagation of IP exchange spin-splitting, in turn limiting the transition-state enhancement of QP iSHE. Contrary to the magnon devices with Nb (BCS SC)

https://doi.org/10.1021/acsnano.1c07192
ACS Nano 2021, 15, 16819−16827

detectors,[14] the maximum enhancement does not appear at $t_{NbSe_2} \approx \xi^{\perp}_{NbSe_2}$ but at a different critical thickness over which the IP crystal symmetry is recovered and so the OOP Ising pairing is no longer protected, allowing the IP exchange field to penetrate. This result should be taken into account for better proximity engineering of Ising SC triplet Josephson junctions with IP ferromagnets.[45] We believe that, with the layer thickness-tunable OOP Cooper pairing[20,40] and IP exchange spin-splitting, 2D Ising SC/FMI bilayers have desirable material properties for the topological protection of spin-polarized triplet Cooper pairs[25] and Majorana Fermions.[26,27] Our findings, together with recent progress in 2D SCs and magnetic vdW crystals,[22,24] also raise the possibility of developing highly efficient atomically thin spin-to-charge converters via symmetry engineering.

METHODS

Device Fabrication. We fabricated the magnon spin-transport devices (Figure 1c,e,g,i) based on 200 nm thick single-crystalline YIG films (from Matesy GmbH, https://www.matesy.de/en/products/materials/yig-single-crystal) as follows. We first defined a pair of Pt electrodes with an area of $1.5 \times 50\ \mu m^2$, which were deposited by dc magnetron plasma sputtering at an Ar pressure of 4×10^{-3} mbar. These Pt electrodes are separated by a center-to-center distance d^{Pt-Pt} of 15 μm, which is comparable to the magnon spin-diffusion length l^{m}_{sd} estimated from our previous study.[14] For the reference device (Figure 1i), we defined the central 15 nm thick Nb detector with a lateral dimension of $9 \times 12\ \mu m^2$, which was grown by Ar-ion beam sputtering at a working pressure of 1.5×10^{-4} mbar. Subsequently, we defined the outer Au(80 nm)/Ru(2 nm) leads and bonding pads, which were deposited by Ar-ion beam sputtering.

We next selected $NbSe_2$ flakes of suitable geometry and thickness, which were mechanically exfoliated from a high-quality single crystal (from HQ Graphene, http://www.hqgraphene.com/NbSe2.php) and first transferred onto SiO_2(300 nm)/Si substrates, via optical microscopy inspection. We then picked up the selected $NbSe_2$ flake and transferred it onto the central region of each magnon device (Figure 1c,e,g) using a polydimethylsiloxane-based dry transfer method (see Supplementary section 1 for full details). All these processes have been conducted in an inert atmosphere glovebox to prevent oxidation and degradation of the 2H-$NbSe_2$. Note that the 2H-$NbSe_2$ flakes and Nb thin film were prepared on the same-piece YIG film, confirming almost identical SHE/iSHE properties of the Pt injectors/detectors.

To prevent the unintentional contribution of iSHE from inner Au/Ru leads themselves to total voltage signals, we electrically isolate them from the active regime of magnon spin-transport by depositing a 10 nm thick Al_2O_3 oxide layer in-between apart from the electrical contact parts on top of the central 2H-$NbSe_2$ (or Nb). Finally, we defined the inner Au(10 nm)/Ru(2 nm) leads, which were deposited by Ar-ion beam sputtering. Before depositing the inner Au/Ru leads, the $NbSe_2$ (or Nb) and Pt surface were gently Ar-ion beam etched for transparent electrical contacts between them.

Superconducting Transition Measurement. To characterize superconducting properties, dc electrical transport measurements were conducted on either transferred $NbSe_2$ flakes or deposited Nb thin films of the fabricated magnon devices attached on either IP (Figure 2b) or OOP (Figure 2c) rotatable holder in a Quantum Design Physical Property Measurement System (PPMS). Using electrical leads 3−6 (Figure 1c,e,g,i) with a four-probe configuration, we measured the resistance R *versus* temperature T curves at the applied current $I \leq 10\ \mu$A while decreasing T. The T-dependent IP (OOP) upper critical field $\mu_0 H^{\parallel}_{c2}$ ($\mu_0 H^{\perp}_{c2}$) of Figure 2d (Figure 2g) was obtained by applying an external magnetic field $\mu_0 H^{\parallel}$ ($\mu_0 H^{\perp}$) parallel (perpendicular) to the interface plan. The $\mu_0 H^{\parallel}_{c2}(T)$ and $\mu_0 H^{\perp}_{c2}(T)$ values are determined from the point where $R = 0.5R_{T=8K}$.

We estimated the $\xi^{\parallel}_{NbSe_2}$ and $\xi^{\perp}_{NbSe_2}$ values of the transferred 2H-$NbSe_2$ flake (t_{NbSe_2} = 9 nm) from the $\mu_0 H^{\parallel}_{c2}(T)$ and $\mu_0 H^{\perp}_{c2}(T)$ data (Figure 2d), respectively, using an anisotropic GL theory[39] for $t_{NbSe_2} \gg \xi^{\perp}_{NbSe_2}$:

$$\mu_0 H^{\parallel}_{c2} = \frac{\Phi_0}{2\pi \xi^{\parallel}_{NbSe_2} \xi^{\perp}_{NbSe_2}} \left(1 - \frac{T}{T_c}\right) \tag{1a}$$

$$\mu_0 H^{\perp}_{c2} = \frac{\Phi_0}{2\pi (\xi^{\parallel}_{NbSe_2})^2} \left(1 - \frac{T}{T_c}\right) \tag{1b}$$

where $\Phi_0 = \frac{h}{2e} = 2.07 \times 10^{-15} Tm^2$ is the magnetic flux quantum. It is noteworthy that as t_{NbSe_2} is reduced and reaches the atomically thin limit ($t_{NbSe_2} \ll \xi^{\perp}_{NbSe_2}$), the dominant Cooper-pair breaking mechanism under application of $\mu_0 H^{\parallel}$ changes from Abrikosov vortex occupation to Ising SOC as recently discussed.[17−21] For $t_{NbSe_2} \ll \xi^{\perp}_{NbSe_2}$, eq 1a can thus be rewritten as

$$\mu_0 H^{\parallel}_{c2} = \sqrt{\mu_0 H^{Ising}_{SO} \mu_0 H^{BCS}_{P} \left(1 - \frac{T}{T_c}\right)} \tag{1c}$$

where $\mu_0 H^{Ising}_{SO}$ is the strength of Ising SO field. For completeness, we also fitted the $\mu_0 H^{\parallel}(T_c)$ data (violet solid line, Figure 2d) with this formula.

On the other hand, for the deposited Nb thin film of t_{Nb} = 15 nm $\leq \xi^{\perp}_{Nb} = \xi^{\parallel}_{Nb}$, the T-dependent upper critical fields (Figure 2h) were fitted with[39]

$$\mu_0 H^{\parallel}_{c2} = \frac{\Phi_0 \sqrt{12}}{2\pi \xi^{\parallel}_{Nb} t_{Nb}} \sqrt{\left(1 - \frac{T}{T_c}\right)} \tag{2a}$$

$$\mu_0 H^{\perp}_{c2} = \frac{\Phi_0}{2\pi (\xi^{\parallel}_{Nb})^2} \left(1 - \frac{T}{T_c}\right) \tag{2b}$$

Note that, unlike bulk Nb, the occupation energy of Abrikosov vortices in a superconducting Nb thin film ($t_{Nb} \leq \xi^{\perp}_{Nb} = \xi^{\parallel}_{Nb}$) under $\mu_0 H^{\parallel}$ is higher than that under $\mu_0 H^{\perp}$, differentiating formulas (eq 2a and 2b) for the T-dependent IP/OOP upper critical fields.[39] This is because the density of Cooper pairs cannot change much on a length scale shorter than the coherence length and hence IP Abrikosov vortices cannot efficiently accommodate magnetic flux.[39] When the Nb (BCS SC) film becomes sufficiently thin ($t_{Nb} \ll \xi^{\perp}_{Nb} = \xi^{\parallel}_{Nb}$), Abrikosov vortex occupation under $\mu_0 H^{\parallel}$ is strongly suppressed and a $\mu_0 H^{\parallel}$-driven dominant Cooper-pair breaker is now the Pauli paramagnetic effect (*i.e.*, Zeeman spin-splitting).[28] Accordingly, eq 2a can be rewritten by

$$\mu_0 H^{\parallel}_{c2} = \mu_0 H^{BCS}_{P} \sqrt{\left(1 - \frac{T}{T_c}\right)} \tag{2c}$$

Nonlocal Measurements. We measured the nonlocal magnon spin-transport (Figure 1a) on the magnon devices attached on an IP rotatable sample holder in the Quantum Design PPMS at various T between 2 and 300 K. A dc current I_{dc} in the range of 0.1−1 mA was applied to the first Pt using a Keithley 6221 current source, and the nonlocal voltages [$V^{Pt}_{nl}(\alpha)$, $V^{NbSe_2(or\ Nb)}_{nl}(\alpha)$] across the second Pt and the central 2H-$NbSe_2$ (or Nb) are simultaneously recorded as a function of IP magnetic-field-angle α with rotating the IP sample holder by a Keithley 2182A nanovoltmeter. Note that α is defined as the relative angle of $\mu_0 H_{ext}$ ($//M_{YIG}$) to the long axis of two Pt electrodes which are collinear.

The Oersted field $\mu_0 H_{Oe}$ induced from I_{dc} applied to the Pt electrode is estimated using Ampere's law

https://doi.org/10.1021/acsnano.1c07192
ACS Nano 2021, 15, 16819−16827

$$\mu_0 H_{Oe} = \frac{\mu_0 I_{dc}}{2\pi w_{Pt}} \ln\left[1 + \frac{w_{Pt}}{d}\right]$$

Here $\mu_0 = 4\pi \times 10^{-7}$ Tm/A is the permeability of free space, w_{Pt} is the width (1.5 μm) of the Pt electrode, and d is the distance from the Pt/YIG interface. For the maximum I_{dc} = 1.0 mA used, we get $\mu_0 H_{Oe}$ = 0.3−0.4 mT at d = 100 nm and it decreases to 0.02−0.03 mT at d = 7.5 μm. These estimated values are *too weak* to perturb the magnetization direction of ferrimagnetic insulating YIG[14] under application of $\mu_0 H^{\|}$ = 5 mT (Figure 1c,e,g,i) and to suppress the superconducting properties of 2H-$NbSe_2$ flakes and a Nb thin film whose upper critical fields in the transition state are larger than 0.5 T (Figure 2b,c,f,g).

ASSOCIATED CONTENT

Supporting Information

The Supporting Information is available free of charge at https://pubs.acs.org/doi/10.1021/acsnano.1c07192.

Dry transfer of 2H-$NbSe_2$ flakes onto magnon spin-transport devices, Nonlocal spin signals detected by the Pt detector across T_c of the 2H-$NbSe_2$ flake, Transition-state enhancement of QP iSHE for the t_{NbSe_2} = 2.5 nm device (PDF)

AUTHOR INFORMATION

Corresponding Authors

Kun-Rok Jeon − *Max Planck Institute of Microstructure Physics, 06120 Halle (Saale), Germany;* orcid.org/0000-0003-0237-990X; Email: jeonkunrok@gmail.com

Stuart S. P. Parkin − *Max Planck Institute of Microstructure Physics, 06120 Halle (Saale), Germany;* Email: stuart.parkin@halle-mpi.mpg.de

Authors

Kyungjune Cho − *Max Planck Institute of Microstructure Physics, 06120 Halle (Saale), Germany*

Anirban Chakraborty − *Max Planck Institute of Microstructure Physics, 06120 Halle (Saale), Germany*

Jae-Chun Jeon − *Max Planck Institute of Microstructure Physics, 06120 Halle (Saale), Germany*

Jiho Yoon − *Max Planck Institute of Microstructure Physics, 06120 Halle (Saale), Germany*

Hyeon Han − *Max Planck Institute of Microstructure Physics, 06120 Halle (Saale), Germany;* orcid.org/0000-0002-2973-5225

Jae-Keun Kim − *Max Planck Institute of Microstructure Physics, 06120 Halle (Saale), Germany*

Complete contact information is available at: https://pubs.acs.org/10.1021/acsnano.1c07192

Author Contributions

†K.-R.J. and K.C. contributed equally to this work. K.-R.J. and S.P.P.P. conceived and designed the experiments. The magnon spin-transport devices were fabricated by K.-R.J. with help from J.Y., J.-C.J., A.C., H.H., J.-K.K., and K.C. K.-R.J. performed exfoliation/pick-up/transfer of 2H-$NbSe_2$ under the guidance of K.C. The nonlocal transport measurements were carried out by K.-R.J. with the help of J.Y. and J.-C.J. K.-R.J. performed the data analysis. S.P.P.P. supervised the project. All authors discussed the results and commented on the manuscript, which was written by K.-R.J., K.C., and S.S.P.P.

Funding

Open access funded by Max Planck Society.

Notes

The authors declare no competing financial interest.

ACKNOWLEDGMENTS

This work was supported by the Alexander von Humboldt Foundation.

REFERENCES

(1) Beckmann, D. Spin Manipulation in Nanoscale S uperconductors. *J. Phys.: Condens. Matter* **2016**, *28*, 163001.

(2) Bergeret, F. S.; Silaev, M.; Virtanen, P.; Heikkilä, T. T. *Colloquium*: Nonequilibrium Effects in Superconductors with a Spin-Splitting Field. *Rev. Mod. Phys.* **2018**, *90*, 041001.

(3) Quay, C. H. L.; Aprili, M. Out-of-Equilibrium Spin Transport in Mesoscopic Superconductors. *Philos. Trans. R. Soc., A* **2018**, *376*, 20150342.

(4) Linder, J.; Robinson, J. W. A. Superconducting Spintronics. *Nat. Phys.* **2015**, *11*, 307.

(5) Yang, H.; Yang, S.-H.; Takahashi, S.; Maekawa, S.; Parkin, S. S. P. Extremely Long Quasiparticle Spin Lifetimes in Superconducting Aluminium Using MgO Tunnel Spin Injectors. *Nat. Mater.* **2010**, *9*, 586.

(6) Wakamura, T.; Akaike, H.; Omori, Y.; Niimi, Y.; Takahashi, S.; Fujimaki, A.; Maekawa, A.; Otani, Y. Quasiparticle-Mediated Spin Hall Effect in a Superconductor. *Nat. Mater.* **2015**, *14* (2015), 675.

(7) Hubler, F.; Lemyre, J. C.; Beckmann, D.; v. Löhneysen, H. Charge Imbalance in Superconductors in the Low-Temperature Limit. *Phys. Rev. B: Condens. Matter Mater. Phys.* **2010**, *81*, 184524.

(8) Hübler, F.; Wolf, M. J.; Beckmann, D.; v. Löhneysen, H. Long-Range Spin-Polarized Quasiparticle Transport in Mesoscopic Al Superconductors with a Zeeman Splitting. *Phys. Rev. Lett.* **2012**, *109*, 207001.

(9) Quay, C. H. L.; Chevallier, D.; Bena, C.; Aprili, M. Spin Imbalance and Spin-Charge Separation in a Mesoscopic Superconductor. *Nat. Phys.* **2013**, *9*, 84.

(10) Silaev, M.; Virtanen, P.; Bergeret, F. S.; Heikkilä, T. T. Long-Range Spin Accumulation from Heat Injection in Mesoscopic Superconductors with Zeeman Splitting. *Phys. Rev. Lett.* **2015**, *114*, 167002.

(11) Machon, P.; Eschrig, M.; Belzig, W. Nonlocal Thermoelectric Effects and Nonlocal Onsager Relations in a Three-Terminal Proximity-Coupled Superconductor-Ferromagnet Device. *Phys. Rev. Lett.* **2013**, *110*, 047002.

(12) Kolenda, S.; Wolf, M. J.; Beckmann, D. Observation of Thermoelectric Currents in High-Field Superconductor-Ferromagnet Tunnel Junctions. *Phys. Rev. Lett.* **2016**, *116*, 097001.

(13) Kuzmanović, M.; Wu, B. Y.; Weideneder, M.; Quay, C. H. L.; Aprili, M. Evidence for Spin-Dependent Energy Transport in a Superconductor. *Nat. Commun.* **2020**, *11*, 4336.

(14) Jeon, K.-R.; Jeon, J.-C.; Zhou, X.; Migliorini, A.; Yoon, J.; Parkin, S. S. P. Giant Transition-State Quasiparticle Spin-Hall Effect in an Exchange-Spin-Split Superconductor Detected by Nonlocal Magnon Spin Transport. *ACS Nano* **2020**, *14*, 15874.

(15) Sinova, J.; Valenzuela, S. O.; Wunderlich, J.; Back, C. H.; Jungwirth, T. Spin Hall Effects. *Rev. Mod. Phys.* **2015**, *87*, 1213.

(16) Ojajärvi, R.; Heikkilä, T. T.; Virtanen, P.; Silaev, M. A. Giant Enhancement to Spin Battery Effect in Superconductor/Ferromagnetic Insulator Systems. *Phys. Rev. B: Condens. Matter Mater. Phys.* **2021**, *103*, 224524.

(17) Xu, X.; Yao, W.; Xiao, D.; Heinz, T. F. Spin and Pseudospins in Layered Transition Metal Dichalcogenides. *Nat. Phys.* **2014**, *10*, 343.

(18) Lu, J. M.; Zheliuk, O.; Leermakers, I.; Yuan, N. F. Q.; Zeitler, U.; Law, K. T.; Ye, J. T. Evidence for Two-Dimensional Ising Superconductivity in Gated MoS_2. *Science* **2015**, *350*, 1353.

(19) Saito, Y.; Nakamura, Y.; Bahramy, M. S.; Kohama, Y.; Ye, J.; Kasahara, Y.; Nakagawa, Y.; Onga, M.; Tokunaga, M.; Nojima, T.; Yanase, Y.; Iwasa, Y. Superconductivity Protected by Spin−Valley Locking in Ion-Gated MoS_2. *Nat. Phys.* **2016**, *12*, 144.

(20) Xi, X.; Wang, Z.; Zhao, W.; Park, J.-H.; Law, K. T.; Berger, H.; Forró, L.; Shan, J.; Mak, K. F. Ising Pairing in Superconducting $NbSe_2$ Atomic Layers. *Nat. Phys.* **2016**, *12*, 139.
(21) Smidman, M.; Salamon, M. B.; Yuan, H. Q.; Agterberg, D. F. Superconductivity and Spin-Orbit Coupling in Non-Centrosymmetric Materials: A Review. *Rep. Prog. Phys.* **2017**, *80*, 036501.
(22) Novoselov, K. S.; Mishchenko, A.; Carvalho, A.; Castro Neto, A. H. 2D Materials and van der Waals Heterostructures. *Science* **2016**, *353*, aac9439.
(23) Lin, X.; Yang, W.; Wang, K. L.; Zhao, W. Two-Dimensional Spintronics for Low-Power Electronics. *Nat. Electron.* **2019**, *2*, 274.
(24) Ghiasi, T. S.; Kaverzin, A. A.; Dismukes, A. H.; de Wal, D. K.; Roy, X.; van Wees, B. J. Electrical and Thermal Generation of Spin Currents by Magnetic Bilayer Graphene. *Nat. Nanotechnol.* **2021**, *16*, 788.
(25) Wickramaratne, D.; Khmelevskyi, S.; Agterberg, D. F.; Mazin, I. I. Ising Superconductivity and Magnetism in $NbSe_2$. *Phys. Rev. X* **2020**, *10*, 041003.
(26) Hsu, Y.-T.; Vaezi, A.; Fischer, M. H.; Kim, E.-A. Topological Superconductivity in Monolayer Transition Metal Dichalcogenides. *Nat. Commun.* **2017**, *8*, 14985.
(27) Vaitiekėnas, S.; Liu, Y.; Krogstrup, P.; Marcus, C. M. Zero-Field Topological Superconductivity in Ferromagnetic Hybrid Nanowires. *Nat. Phys.* **2021**, *17*, 43.
(28) Clogston, A. M. Upper Limit for the Critical Field in Hard Superconductors. *Phys. Rev. Lett.* **1962**, *9*, 266.
(29) de Trey, P.; Gygax, S.; Jan, J. P. Anisotropy of Ginzburg–Landau Parameter κ in $NbSe_2$. *J. Low Temp. Phys.* **1973**, *11*, 421.
(30) Marezio, M.; Dernier, P. D.; Menth, A.; Hull, G. W., Jr. The Crystal Structure of $NbSe_2$ at 15 K. *J. Solid State Chem.* **1972**, *4*, 425.
(31) Mattheiss, L. F. Band Structures of Transition-Metal-Dichalcogenide Layer Compounds. *Phys. Rev. B* **1973**, *8*, 3719.
(32) Buzdin, A. I. Proximity Effects in Superconductor-Ferromagnet Heterostructures. *Rev. Mod. Phys.* **2005**, *77*, 935.
(33) Žutić, I.; Matos-Abiague, A.; Scharf, B.; Dery, H.; Belashchenko, K. Proximitized Materials. *Mater. Today* **2019**, *22*, 85.
(34) Qiu, D.; Gong, C.; Wang, S.; Zhang, M.; Yang, C.; Wang, X.; Xiong, J. Recent Advances in 2D Superconductors. *Adv. Mater.* **2021**, *33*, 2006124.
(35) Ganzhorn, K.; Wimmer, T.; Cramer, J.; Schlitz, R.; Geprägs, S.; Jakob, G.; Gross, R.; Huebl, H.; Kläui, M.; Goennenwein, S. T. B. Temperature Dependence of the Non-Local Spin Seebeck Effect in YIG/Pt Nanostructures. *AIP Adv.* **2017**, *7*, 085102.
(36) Cornelissen, L. J.; Liu, J.; Duine, R. A.; Ben Youssef, J.; van Wees, B. J. Long-Distance Transport of Magnon Spin Information in a Magnetic Insulator at Room Temperature. *Nat. Phys.* **2015**, *11*, 1022.
(37) Xi, X.; Zhao, L.; Wang, Z.; Berger, H.; Forró, L.; Shan, J.; Mak, K. F. Strongly Enhanced Charge-Density-Wave Order in Monolayer $NbSe_2$. *Nat. Nanotechnol.* **2015**, *10*, 765.
(38) McKenzie, R. H. Is the Ground State of Alpha-(BEDT-TTF)2MHg(SCN)4[M = K,Rb,Tl] a Charge-Density Wave or a Spin-Density Wave? *arXiv (Strongly Correlated Electrons)*, March 5, **1998**, ver. 2. https://arxiv.org/abs/cond-mat/9706235v2.
(39) Tinkham, M. *Introduction to Superconductivity*, 2nd ed.; McGraw-Hill: New York, 1996.
(40) de la Barrera, S. C.; Sinko, M. R.; Gopalan, D. P.; Sivadas, N.; Seyler, K. L.; Watanabe, K.; Taniguchi, T.; Tsen, A. W.; Xu, X.; Xiao, D.; Hunt, B. M. Tuning Ising Superconductivity with Layer and Spin–Orbit Coupling in Two-Dimensional Transition-Metal Dichalcogenides. *Nat. Commun.* **2018**, *9*, 1427.
(41) Wei, P.; Lee, S.; Lemaitre, F.; Pinel, L.; Cutaia, D.; Cha, W.; Katmis, F.; Zhu, Y.; Heiman, D.; Hone, J.; Moodera, J. S.; Chen, C.-T. Strong Interfacial Exchange Field in the Graphene/EuS Heterostructure. *Nat. Mater.* **2016**, *15*, 711.
(42) Kato, T.; Ohnuma, Y.; Matsuo, M.; Rech, J.; Jonckheere, T.; Martin, T. Microscopic Theory of Spin Transport at the Interface between a Superconductor and a Ferromagnetic Insulator. *Phys. Rev. B: Condens. Matter Mater. Phys.* **2019**, *99*, 144411.
(43) Dvir, T.; Massee, F.; Attias, L.; Khodas, M.; Aprili, M.; Quay, C. H. L.; Steinberg, H. Spectroscopy of Bulk and Few-Layer Superconducting $NbSe_2$ with van der Waals Tunnel Junctions. *Nat. Commun.* **2018**, *9*, 598.
(44) Xing, W.; Qiu, L.; Wang, X.; Yao, Y.; Ma, Y.; Cai, R.; Jia, S.; Xie, X. C.; Han, W. Magnon Transport in Quasi-Two-Dimensional van der Waals Antiferromagnets. *Phys. Rev. X* **2019**, *9*, 011026.
(45) Tang, G.; Klees, R. L.; Bruder, C.; Belzig, W. Controlling Charge and Spin Transport in an Ising-Superconductor Josephson Junction. *arXiv (Mesoscale and Nanoscale Physics)*, July 29, **2021**, ver. 1. https://arxiv.org/abs/2107.14259.

https://doi.org/10.1021/acsnano.1c07192
ACS Nano 2021, 15, 16819–16827